Maximal Quantum Interaction between Free Electrons and Photons

Zetao Xie,[1,*] Zeling Chen,[1,*] Hao Li,[2] Qinghui Yan,[3,4] Hongsheng Chen,[3] Xiao Lin,[3]
Ido Kaminer,[4] Owen D. Miller,[2,†] and Yi Yang[1,‡]
[1]*Department of Physics and HK Institute of Quantum Science and Technology,*
The University of Hong Kong, Pokfulam, Hong Kong, China
[2]*Department of Applied Physics and Energy Sciences Institute, Yale University, New Haven, Connecticut 06520, USA*
[3]*Interdisciplinary Center for Quantum Information, State Key Laboratory of Modern Optical Instrumentation,*
College of Information Science and Electronic Engineering, Zhejiang University, Hangzhou 310027, China
[4]*Solid State Institute and Faculty of Electrical and Computer Engineering,*
Technion—Israel Institute of Technology, 32000 Haifa, Israel

(Received 3 April 2024; revised 19 July 2024; accepted 27 August 2024; published 31 January 2025)

The emerging field of free-electron quantum optics enables electron-photon entanglement and holds the potential for generating nontrivial photon states for quantum information processing. Although recent experimental studies have entered the quantum regime, rapid theoretical developments predict that qualitatively unique phenomena only emerge beyond a certain interaction strength. It is thus pertinent to identify the maximal electron-photon interaction strength and the materials, geometries, and particle energies that enable one to approach it. We derive an upper limit to the quantum vacuum interaction strength between free electrons and single-mode photons, which illuminates the conditions for the strongest interaction. Crucially, we obtain an explicit energy selection recipe for electrons and photons to achieve maximal interaction at arbitrary separations and identify two optimal regimes favoring either fast or slow electrons over those with intermediate velocities. We validate the limit by analytical and numerical calculations on canonical geometries and provide near-optimal designs indicating the feasibility of strong quantum interactions. Our findings offer fundamental intuition for maximizing the quantum interaction between free electrons and photons and provide practical design rules for future experiments on electron-photon and electron-mediated photon-photon entanglement. They should also enable the evaluation of key metrics for applications such as the maximum power of free-electron radiation sources and the maximum acceleration gradient of dielectric laser accelerators.

DOI: 10.1103/PhysRevLett.134.043803

Free-electron-light interaction with structured optical environments leads to photon emission through diverse radiation mechanisms [1–7]. These interaction processes lie at the heart of modern electron microscopy [1–3], spectroscopy [8], radiation sources [9–12], particle detection [13,14], free-electron lasers [15], accelerators [16–19], and biomedical imaging [20,21]. Recent theoretical advances have shown that the quantum-photonic nature of light could become critical for describing the interaction [22,23]. It was further predicted that the interaction could shape and entangle electron and photon wave functions [22,24–30], and induce entanglement among electrons [22] and photons [31] themselves. The interaction has also been proposed for free-electronic topological probes and quantum simulators [32–34]. Such a wide range of predicted quantum-optical interactions now form the basis of free-electron quantum optics.

With the rapid developments of photon-induced near-field electron microscopy (PINEM) [35–37] on photonic platforms [38–41], the predicted quantum free-electron-light interaction has been realized in a few experiments [42–44]. The crucial parameters for these interactions are the dimensionless spontaneous coupling strength g_{Q} with vacuum and its stimulated counterpart g with external optical fields (g_{Q} and g are sometimes respectively denoted as β_0 and β in the literature, e.g., Refs. [2,23,45]). g_{Q} can be calculated via the spectral integration of spontaneous electron energy loss [22,23,27,28,46,47], and the two parameters relate to each other via $g = \sqrt{N} g_{\mathrm{Q}}$ for coherent states where N is the number of photons injected into the optical mode from a pump laser [22,23]. In particular, the vacuum spontaneous processes exhibit intriguing prospects for universal and ultrafast quantum computation and information processing because they can create a variety of highly nontrivial quantum optical states under designed interaction sequences [47,48] and they are essential for the proposed hybrid free-electron-polariton blockade [49].

---

[*] Z. X. and Z. C. contributed equally to this Letter.
[†] Contact author: owen.miller@yale.edu
[‡] Contact author: yiyg@hku.hk

The key to these predictions is a strong quantum interaction with $|g_\mathrm{Q}| > 1$. Intuitively, this regime indicates that each emitted photon can cycle back to the electron and cause a cascade of multiphoton emission and absorption. This strong interaction regime involves higher-order quantum electrodynamics processes and can be understood as a unique type of optical nonlinearity. Strong optical nonlinearities are being pursued in all fields of photonics, with the goal of reaching single-photon nonlinearities. Thus, a question of fundamental importance is whether electron-photon interactions can reach this regime. Answering this question requires an upper limit to g_Q in arbitrary photonic environments.

We begin the analysis by considering an electron beam at normalized velocity $\beta = v/c$, interacting with an arbitrary photonic structure characterized by volume V and material permittivity $\epsilon(\mathbf{r},\omega)$ in its near field with a separation d, as shown in Fig. 1. Photon exchanges between the electron and the structure can be strongly amplified when the photonic structure supports modes with large spatial and spectral overlap with the electron's excitation field. In the framework of quantum optics, the joint electron (e$^-$)-photon (ph) state $|\Psi\rangle = |\psi^\mathrm{e}\rangle \otimes |\psi^\mathrm{ph}\rangle = \sum_{n=0}^{\infty}\sum_{k=-\infty}^{+\infty} c_{n,k}|E_k, n\rangle$ is a superposition state with electron energy $E_0 + k\hbar\omega$ and n photons where n denotes the photonic Fock states and k denotes the electronic energy ladder. For spontaneous processes with an electron of energy E_0 in an empty cavity, the initial state is $|\Psi_\mathrm{i}\rangle = |E_0, 0\rangle$, and the final state $|\Psi_\mathrm{f}\rangle$ satisfies $n = -k$ by virtue of energy conservation. The initial and final states are related by the scattering matrix, represented as $|\Psi_\mathrm{f}\rangle = \hat{S}|\Psi_\mathrm{i}\rangle$, which is given by [22,23]

$$\hat{S} = \exp\left(g_\mathrm{Q}\hat{b}^\dagger\hat{a} - g_\mathrm{Q}^*\hat{b}\hat{a}^\dagger\right), \tag{1}$$

where $\hat{a}$, $\hat{a}^\dagger$ are the annihilation and creation operators of the optical mode; $\hat{b}$, $\hat{b}^\dagger$ denote the ladder operators for electron energy; and g_Q is the dimensionless electron-photon interaction strength. In the limit of vacuum zero field [50], the quantum-optical theory of PINEM coincides with the theory of electron energy loss spectroscopy (EELS), which enables the calculation of g_Q from the spectrally integrated electron energy loss probability [see Supplemental Material (SM) [51], Sec. S1]: $|g_\mathrm{Q}|^2 = \int \Gamma(\omega)\mathrm{d}\omega$ without competing loss mechanisms [27,28,46,47]. In stimulated processes like PINEM, the general quantum framework still holds, whereas one should replace g_Q with the stimulated strength g amplified by the input coherent state amplitude.

To impose a bound on g_Q and g, we treat free electrons interacting with an arbitrary photonic environment as an electromagnetic scattering problem (Fig. 1). Although this scattering perspective has previously led to a single-frequency (zero-bandwidth) limit [52], it cannot translate to a g_Q limit straightforwardly because of a divergent material metric for lossless materials. Alternatively, a sum-rule approach can bound near-field interactions (e.g., power loss from a stationary point dipole) [53,54], but its applicability to free electrons is hindered by the nonanalytic behaviors of their external fields near the complex-plane origin. Recently, a $\mathbb{T}$-matrix-based oscillator representation framework [55] (where the $\mathbb{T}$ operator relates the polarization fields with incident fields [56,57]) appears ideal for analyzing free-electron-light scattering.

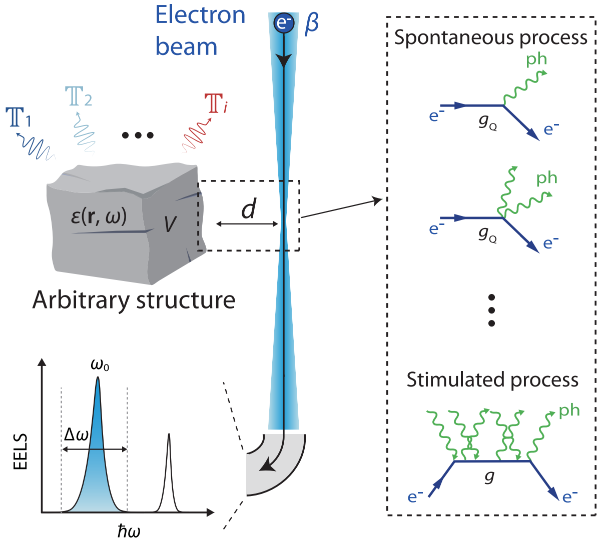

FIG. 1. Theoretical framework. An electron of velocity $\beta = v/c$ traveling close to an arbitrary structure at a separated distance d. The structure is defined by material permittivity $\epsilon(\mathbf{r},\omega)$ within a volume V. The electron (e$^-$) can become an entangled state with its emitted photons (ph) through spontaneous or stimulated processes of interaction strength g_Q and g, respectively. The interaction can be described by an oscillator representation of the scattering $\mathbb{T}$ matrix.

In the polarization-response representation, the frequency-dependent extinction (i.e., energy loss of free electrons) equals the work done by the incident field on the induced polarization field in the scatterer, $P_\mathrm{ext}(\omega) = (\omega/2)\mathrm{Im}\int_V \mathbf{E}_\mathrm{inc}^* \cdot \mathbf{P}\mathrm{d}V$. $\mathbf{E}_\mathrm{inc}$ is the incident field generated by free electrons [1],

$$\mathbf{E}_\mathrm{inc}(\mathbf{r},\omega) = \frac{e\kappa_\rho \mathrm{e}^{\mathrm{i}k_v x}}{2\pi\omega\epsilon_0}\left[\mathrm{i}\kappa_\rho K_0(\kappa_\rho\rho)\hat{\mathbf{x}} - k_v K_1(\kappa_\rho\rho)\hat{\boldsymbol{\rho}}\right], \tag{2}$$

where ϵ_0 is the vacuum permittivity, $k = \omega/c$, $k_v = \omega/v$, $\kappa_\rho = \sqrt{k_v{}^2 - k^2}$ are the free-space, electron longitudinal, and transverse wave vectors, respectively, and K_n is the nth-order modified Bessel function of the second kind.

The polarization response is related to the incident field through a linear operator, the "$\mathbb{T}$ matrix" [56]: $\mathbf{P}(\mathbf{r}) = \int_V \mathbb{T}(\mathbf{r},\mathbf{r}')\cdot\mathbf{E}_\mathrm{inc}(\mathbf{r}')\mathrm{d}\mathbf{r}'$, or $\mathbf{p} = \mathbb{T}\mathbf{e}_\mathrm{inc}$ in vector-matrix notation that we use throughout. $\mathbb{T}$ matrix relates to the Green function formalism via $\mathbb{T} = [\chi^{-1} - \mathbb{G}_0]^{-1}$, where χ is material electric susceptibility and $\mathbb{G}_0$ is the free-space Green function (see SM, Sec. S2.A). Here, we work with nonmagnetic materials with unit permeability (see discussions in SM, Sec. S12). Causality and passivity produce a Kramers-Kronig relation and sum-rule constraints for the $\mathbb{T}$ matrix. These properties enable the decomposition of the $\mathbb{T}$ matrix into an infinite sum of lossless Drude-Lorentz oscillators with resonance frequency ω_i and highly constrained matrix-valued oscillator strengths $\mathbb{T}_i$ representing the only degrees of freedom [55] (see Sec. S2). Contributions from $\mathbb{T}_i$ at well-separated ω_i originate from different modes, including resonances in the upper half of the complex frequency plane or guided modes on its real axis. For reciprocal systems, combining the zero-frequency sum rule, the oscillator representation, and the domain monotonicity of polarizability [53] along the positive-frequency axis yields $\omega \mathrm{Im}\mathbb{T}(\omega) \le (\pi\tau/2)\sum_{i=1}^{\infty}\omega^2\mathbb{T}_i\delta(\omega-\omega_i)$, which can reformulate the extinction as

$$P_{\mathrm{ext}}(\omega) \le \frac{\omega^2\pi\epsilon_0\tau}{4}\sum_{i=1}^{\infty}\mathbf{e}_{\mathrm{inc}}^{\dagger}\mathbb{T}_i\mathbf{e}_{\mathrm{inc}}\delta(\omega-\omega_{\mathrm{i}}). \tag{3}$$

The constant τ is a dimensionless electrostatic permittivity coefficient relating the incident and total fields at zero frequency via $\mathbf{P}(0) = \epsilon_0\tau\mathbf{E}_{\mathrm{inc}}(0)$.

Based on this foundation, we next derive the upper limit to the vacuum strength g_{Q} of free-electron-photon interaction. Under certain interaction bandwidth described by a dimensionless window function $\Theta(\omega;\omega_0,\Delta\omega) \le 1$ (peaked at ω_0 with bandwidth $\Delta\omega$), g_{Q} can be evaluated by integrating the loss probability $\Gamma(\omega) = P_{\mathrm{ext}}(\omega)/\hbar\omega$: $|g_{\mathrm{Q}}|^2 = \int\Gamma(\omega)\Theta(\omega;\omega_0,\Delta\omega)\mathrm{d}\omega$. By combining Eq. (3), $|g_{\mathrm{Q}}|^2$ becomes

$$|g_{\mathrm{Q}}|^2 \le \frac{\pi\epsilon_0\tau}{4\hbar}\mathrm{Tr}\sum_{i=1}^{\infty}\mathbb{T}_i\mathbb{E}_i, \tag{4}$$

a $\mathbb{T}_i$-weighted sum of $\mathbb{E}_i \equiv \omega_i\mathbf{e}_{\mathrm{inc}}(\omega_i)\mathbf{e}_{\mathrm{inc}}^{\dagger}(\omega_i)\Theta(\omega_i;\omega_0,\Delta\omega)$ that incorporates the frequency of the emitted photons, the incident field, and the window function. Because $\omega\mathbf{e}_{\mathrm{inc}}(\omega)\mathbf{e}_{\mathrm{inc}}^{\dagger}(\omega)$ varies much slower than $\Theta(\omega;\omega_0,\Delta\omega)$ for well-defined quality factors ($\omega_0 \gg \Delta\omega$), $\mathbb{E}_i$ also spectrally peaks at ω_0 with negligible detuning. Therefore, setting $\mathbb{T}_i = \mathbb{I}_V$ for the oscillator at ω_0 and zero elsewhere will maximize Eq. (4), which simultaneously satisfies the sum-rule constraint $\sum_{i=1}^{\infty}\mathbb{T}_i = \mathbb{I}_V$, where $\mathbb{I}_V$ is an identity matrix within the scatterer volume V. This mathematically optimal choice corresponds to the physical condition of all of the sum-rule-constrained polarization responses concentrating within the frequency window of interest.

Applying the single-mode condition at ω_0 to Eq. (4), we get

$$|g_{\mathrm{Q}}|^2 \le \frac{\pi\epsilon_0\omega_0\tau}{4\hbar}\int_V|\mathbf{E}_{\mathrm{inc}}(\omega_0)|^2\mathrm{d}V. \tag{5}$$

This limit to g_{Q} thus becomes a simple product among physical constants, photon frequency, electrostatic polarizability, and the integration of the incident fields within the scatterer. The limit is general: it applies to both isolated structures [see example in Fig. 5(a)] and extended structures [see examples in Figs. 5(b)–5(e)]; it also applies to both guided modes and resonances below and above the light line (see SM, Sec. S2.C). The limit also remains agnostic about the composition of the total energy loss, and, therefore, can also be used for bounding spectrally integrated absorption and coherent cathodoluminescence.

We can obtain τ analytically for free electrons with canonical geometries. For example, $\tau = 2\epsilon_1(\epsilon_2-1)/(\epsilon_2+\epsilon_1)$ for a half-space, $\tau = \epsilon_1(\epsilon_2-1)/\epsilon_2$ for a concentric cylinder, and $\tau_l = (\epsilon_2-1)\epsilon_1(2l+1)/[l(\epsilon_1+\epsilon_2)+\epsilon_1]$ for a sphere, where ϵ_1 and ϵ_2 are "electrostatic" permittivities of materials 1 (background) and 2 (scatter), respectively and l is the order of associated Legendre polynomials; see SM, Sec. S2.D). Evidently, τ is finite and bounded for both dielectrics and perfect conductors (see SM, Sec. S2.D).

We further obtain shape-independent upper limits for line and point electrons by enclosing arbitrary scatterers with canonical geometries. Assuming translational invariance along one of its transverse directions and the spatial coherence of the source current [58], a line-electron beam (sometimes also denoted as "sheet electron beam") is a simplified mathematical treatment used in many free-electron theory analyses [59–63].

Applying Eq. (5) to a line electron beam moving above a half-space (which can enclose an arbitrary scatterer) at a separation d yields a shape-independent limit for 2D line electrons (see SM, Sec. S3),

$$|g_{\mathrm{Q}}|_{\mathrm{2D}}^2 \le \frac{\pi q^2\tau L}{32\hbar\epsilon_0}\frac{(\mathrm{k}_{v,0}^2+\kappa_{\rho,0}^2)}{\omega_0\kappa_{\rho,0}}\mathrm{e}^{-2\kappa_{\rho,0}d}, \tag{6}$$

where q is the charge density per unit transverse length, L is the interaction length, the subscript "0" in k_0, $k_{v,0}$, and $\kappa_{\rho,0}$ [see original definitions in Eq. (2)] denotes the target photon frequency ω_0, and $\gamma = 1/\sqrt{1-\beta^2}$ is the Lorentz factor.

Applying Eq. (5) to a point electron moving at the center of a concentric hollow cylinder sector (which can enclose an arbitrary scatterer) of azimuthal opening angle ψ, inner radius d, and outer radius ∞ leads to a shape-independent limit for point electrons (see SM, Sec. S4),

$$|g_{\mathrm{Q}}|_{\mathrm{3D}}^2 \le \frac{\alpha\tau\psi L}{4c}\frac{\omega_0}{\beta^2}\kappa_{\rho,0}dK_0(\kappa_{\rho,0}d)K_1(\kappa_{\rho,0}d), \tag{7}$$

where α is the fine-structure constant. The limits Eqs. (5)–(7) are the key analytical findings of the Letter. They show that the maximum $|g_{\mathrm{Q}}|$ for a target emission center frequency ω_0 is solely determined by the electron velocity (via β and $\kappa_{\rho,0}$), the separation d, and the electrostatic polarizability τ of the optical environment.

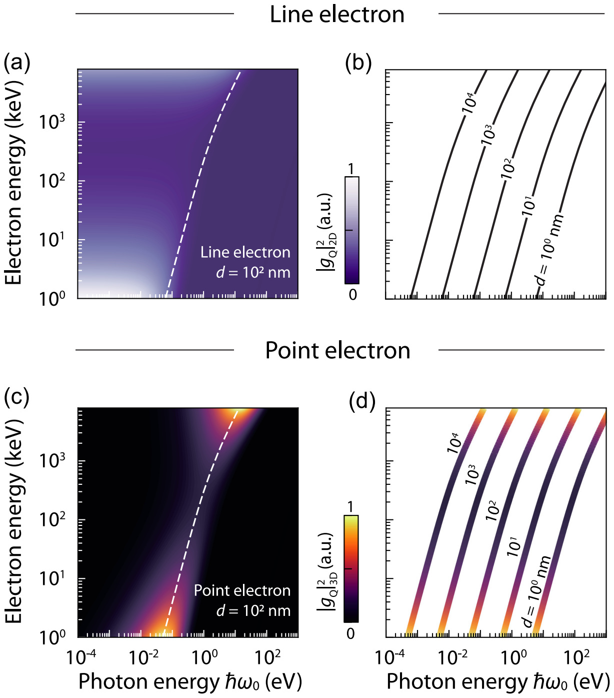

FIG. 2. Universal behaviors of the quantum interaction strength $|g_Q|^2$. (a) Line-electron upper limit Eq. (6) as a function of electron energy and photon energy under a separation distance $d = 100$ nm. (b) Photon energy cutoff of line-electron limit Eq. (8) across various separation d. (c) Point-electron limit Eq. (7) for $d = 100$ nm. (d). The optimal electron and photon energies under different separation d [Eqs. (9) and (10)].

We illustrate the universal behaviors of the quantum upper limits in Fig. 2 to depict the key features of Eqs. (6) and (7), ignoring the fractional prefactors comprising physical constants and structural coefficients. This way, we can obtain a general energy selection recipe under arbitrary separations.

For line electrons [Fig. 2(a)], a photon energy cutoff condition [dashed line in Fig. 2(a); SM, Sec. S5] appears,

$$\kappa_{\rho,0}d = \omega_0 d / c\beta\gamma = 0.5, \tag{8}$$

meaning that large $|g_Q|$ is possible and forbidden below and above the cutoff photon energies, respectively, as indicated by the dichotomy of the brightness and darkness to the left and right of the cutoff line in Fig. 2(a). As the separation distance reduces, the cutoff line blueshifts in photon energy [Fig. 2(b)].

For point electrons [Fig. 2(c)], an optimal condition [dashed line in Fig. 2(c) and see SM, Sec. S6.A] illuminates the choice of electron and photon energies to maximize their interaction,

$$K_0(\kappa_{\rho,0}d)K_1(\kappa_{\rho,0}d) = \kappa_{\rho,0}d[K_0^2(\kappa_{\rho,0}d) + K_1^2(\kappa_{\rho,0}d)]. \tag{9}$$

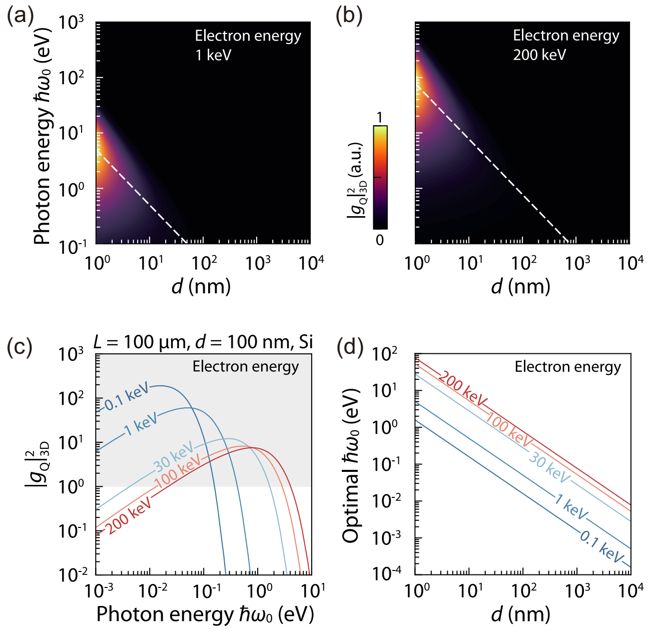

FIG. 3. $|g_Q|^2$ upper limit at typical electron energies. (a), (b) Normalized upper limit for electron energy 1 keV (a) and 200 keV (b), as a function of photon energy and separation. The dashed line indicates the optimal condition Eq. (9). (c) Upper limit for typical electron energies for interaction length $L = 100$ μm and separation $d = 100$ nm. (d) Optimal photon energy versus separation distance.

Such an optimal condition is satisfied under a simple "golden" condition

$$\kappa_{\rho,0}d \approx 0.4064, \tag{10}$$

which differs from line electrons' cutoff condition Eq. (8). In particular, two optimal regimes emerge and favor relativistic [top-right brightness in Fig. 2(c), ultraviolet 10 eV photons coupled to $\gtrsim 6$ MeV electrons when $d = 100$ nm] and nonrelativistic [bottom-left brightness in Fig. 2(c), long-infrared 0.1 eV photons coupled to $\lesssim 4$ keV electrons when $d = 100$ nm] electrons, respectively (see detailed analysis of the optimal regimes in SM, Sec. VI.C). The fast-electron optimal regime aligns with traditional free-electron physics, where high-energy photons are generated with relativistic electrons, whereas the slow-electron optimal regime indicates the huge potential for quantum electron-light interaction with slow electrons, which has been recognized in an early study on multiplasmon generation in graphene [64] and rapid development is being made in more recent years [52,63,65–79]. Nevertheless, associated practical limitations, including electron beam control, energy loss resolution, and optical confinement should be considered (see SM, Sec. S13). For intermediate electron energies, the optimal photon energies can be analogously defined using Eq. (9), although the associated limit is lower than those for the two optima. The

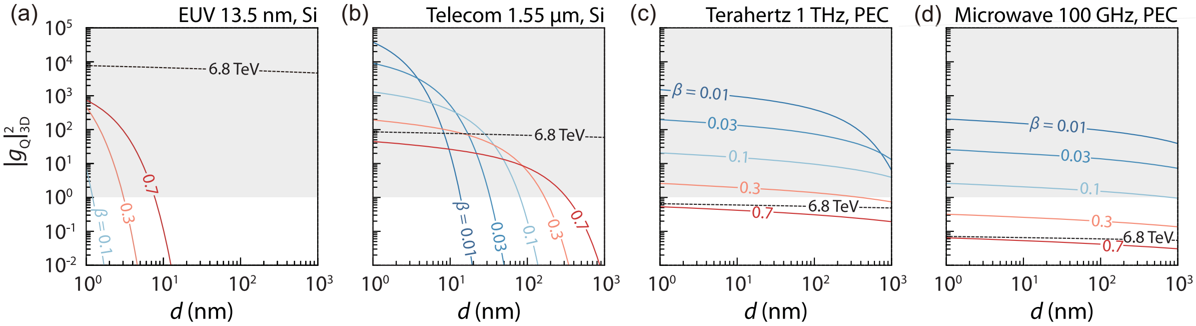

FIG. 4. $|g_Q|^2$ upper limit at typical photon frequencies. We vary electron velocities β and fix the interaction length at 100 μm. The black dashed line represents ultrarelativistic 6.8 TeV electrons. The light gray shading indicates the $|g_Q|^2 > 1$ regime.

two optimal regimes prevail under various separation distances [Fig. 2(d)].

We address the upper limit's behaviors at various electron energies (Fig. 3; see detailed discussion in SM, Sec. S6.B). For electrons of 1 keV and 200 keV, the trajectory of the $|g_Q|^2$ optima [dashed lines in Figs. 3(a) and 3(b)] again follows Eq. (10) for various separations. In Fig. 3(c), we fix $d = 100$ nm and compute the upper limit for various electron energies, illuminating the optimal photon energy selection. Notably, $|g_Q|^2$ caps at ~10 for 200-keV electrons and 1-eV photons that have been prevalently used in modern experiments (assuming interaction length $L = 100$ μm). Figure 3(d) illustrates the optimal photon energies under various separations based on the optimal condition Eq. (10).

We contextualize the discussion by evaluating the feasibility of $|g_Q| > 1$ at concrete frequency windows. Under various electron velocities β and separation d, Fig. 4 shows the $|g_Q|^2$ upper limit for point electrons [Eq. (7)] in four technologically relevant regimes. At the extreme ultraviolet (EUV) 13.5 nm [Fig. 4(a)], despite the high limits near the atomic-scale separations (under which quantum tunneling and surface effects can become pronounced and modify the bounds here [80–82]), $|g_Q| > 1$ is almost impossible for $d \gtrapprox 10$ nm except with $\beta \gtrapprox 0.8$ relativistic electrons. At the telecom 1.55 μm [Fig. 4(b)], whereas slow electrons' upper limits are higher at tens of nanometers or smaller separation, fast electrons with $\beta \gtrapprox 0.3$ are superior at $d \gtrapprox 100$ nm, a typical separation in modern grazing-interaction experiments. Toward the longer wavelengths, the advantages of slow electrons are predominant. $|g_Q| > 1$ is only possible for $\beta \lessapprox 0.3$ and $\beta \lessapprox 0.1$ at 1 THz [Fig. 4(c)] and 100 GHz [Fig. 4(d)], respectively. Despite the $\ln(\gamma)$ divergence of the limit Eq. (7) in electron energy, the slow-electron advantage remains evident when comparing with electrons of 6.8 TeV [dashed lines in Figs. 4(c) and 4(d); see more discussion on its trend in SM, Sec. S6.D], the current highest acceleration energy [83]. Taken together, the $|g_Q| > 1$ goal is indeed challenging for EUV and x-ray photons; nevertheless, slow electrons are promising from electrostatics to the far infrared, and fast electrons are advantageous from mid-infrared to far ultraviolet; the evaluation is based on the current levels of electron beam collimation and focusing (see detailed discussions on each spectral regimes in SM, Sec. S14). In the Appendix, we provide numerical validations and near-optimal designs for the limits.

In summary, we have theoretically derived a universal upper limit to the quantum interaction strength g_Q between free electrons and single-mode photons. The limit allows us to evaluate the feasibility of achieving the $|g_Q| > 1$ strong interaction condition over all possible designs across the electromagnetic spectrum without exhaustive computational optimization. Under arbitrary separations, the limits identify two optimal interaction regimes, showing how to select electron and photon energy to maximize their interaction.

The limits derived here hinge on reciprocity, under which the skew-symmetric part of the $\mathbb{T}$ matrix vanishes, and the sum rule of the real-symmetric part of $\mathbb{T}$ can be applied; it is thus pertinent to generalize the limits to nonreciprocal free-electron systems [84–86] and explore the possibility for higher $|g_Q|$ therein. Relying on the single-mode condition, the limits can be straightforwardly applied to waveguides and fibers whose cross sections are much smaller than the operation wavelengths. As the electron-structure separation increases into the far field, energy loss undergoes exponential decay, and its spectral composition can become multimodal. This scenario may violate the single-mode condition, decrease the coupling ideality, and cause an apparent breakdown of the limits here because the integration of energy loss no longer corresponds to the $|g_Q|^2$ of a particular mode of interest (e.g., when the tail of the zero-loss peak dominates; see SM, Sec. S11). Therefore, it would also be of interest to generalize the present work into the multimodal condition (e.g., a pulse coupled to multiple spectral bands [46], a continuum of transverse modes [11], and a continuum of longitudinal modes [77]). The findings here offer an intuitive understanding of maximizing the quantum interaction between free electrons and photons.

Note added—During the completion of this manuscript, we became aware of related work [87].

Acknowledgments—We thank F. J. García de Abajo, F. J. García-Vidal, Yixin Sha, and Zhexin Zhao for fruitful discussions. The authors acknowledge the support from the National Natural Science Foundation of China Excellent Young Scientists Fund (12222417), the Hong Kong Research Grants Council through Early Career Scheme (27300924) and Strategic Topics grant (STG3/E-704/23-N), the Startup Fund of The University of Hong Kong, the Asian Young Scientist Fellowship, the Croucher Foundation, and the Xplorer Prize. H. L. and O. D. M. were supported by Air Force Office of Scientific Research Grant No. FA9550-22-1-0393 and by the Simons Collaboration on Extreme Wave Phenomena Based on Symmetries (Award No. SFI-MPS-EWP-00008530-09). I. K. was partially supported by the Israel Science Foundation, Grant No. 385/23. X. L. and H. C. were partly supported by NSFC Excellent Young Scientists Fund (Overseas) and under Grants No. 62175212, No. 62475227, No. 11961141010, and No. 61975176; the Key Research and Development Program of the Ministry of Science and Technology under Grants No. 2022YFA1404704, No. 2022YFA1404902, and No. 2022YFA1405200; Zhejiang Provincial Natural Science Fund Key Project under Grant No. LZ23F050003; and the Fundamental Research Funds for the Central Universities under Grant No. 226-2024-00022.

---

[1] F. J. García de Abajo, Rev. Mod. Phys. **82**, 209 (2010).
[2] A. Polman, M. Kociak, and F. J. García de Abajo, Nat. Mater. **18**, 1158 (2019).
[3] F. J. García de Abajo and V. Di Giulio, ACS Photonics **8**, 945 (2021).
[4] N. Talebi, Adv. Phys. **3**, 1499438 (2018).
[5] N. Rivera and I. Kaminer, Nat. Rev. Phys. **2**, 538 (2020).
[6] R. Shiloh, N. Schönenberger, Y. Adiv, R. Ruimy, A. Karnieli, T. Hughes, R. J. England, K. J. Leedle, D. S. Black, Z. Zhao *et al.*, Adv. Opt. Photonics **14**, 862 (2022).
[7] C. Roques-Carmes, S. E. Kooi, Y. Yang, N. Rivera, P. D. Keathley, J. D. Joannopoulos, S. G. Johnson, I. Kaminer, K. K. Berggren, and M. Soljačić, Appl. Phys. Rev. **10** (2023).
[8] N. Varkentina, Y. Auad, S. Y. Woo, A. Zobelli, L. Bocher, J.-D. Blazit, X. Li, M. Tencé, K. Watanabe, T. Taniguchi *et al.*, Sci. Adv. **8**, eabq4947 (2022).
[9] A. Massuda, C. Roques-Carmes, Y. Yang, S. E. Kooi, Y. Yang, C. Murdia, K. K. Berggren, I. Kaminer, and M. Soljačić, ACS Photonics **5**, 3513 (2018).
[10] C. Roques-Carmes, S. E. Kooi, Y. Yang, A. Massuda, P. D. Keathley, A. Zaidi, Y. Yang, J. D. Joannopoulos, K. K. Berggren, I. Kaminer *et al.*, Nat. Commun. **10**, 3176 (2019).
[11] Y. Yang, C. Roques-Carmes, S. E. Kooi, H. Tang, J. Beroz, E. Mazur, I. Kaminer, J. D. Joannopoulos, and M. Soljačić, Nature (London) **613**, 42 (2023).
[12] Z. Gong, J. Chen, R. Chen, X. Zhu, C. Wang, X. Zhang, H. Hu, Y. Yang, B. Zhang, H. Chen *et al.*, Proc. Natl. Acad. Sci. U.S.A. **120**, e2306601120 (2023).
[13] X. Lin, S. Easo, Y. Shen, H. Chen, B. Zhang, J. D. Joannopoulos, M. Soljačić, and I. Kaminer, Nat. Phys. **14**, 816 (2018).
[14] X. Lin, H. Hu, S. Easo, Y. Yang, Y. Shen, K. Yin, M. P. Blago, I. Kaminer, B. Zhang, H. Chen *et al.*, Nat. Commun. **12**, 5554 (2021).
[15] C. Pellegrini, A. Marinelli, and S. Reiche, Rev. Mod. Phys. **88**, 015006 (2016).
[16] N. V. Sapra, K. Y. Yang, D. Vercruysse, K. J. Leedle, D. S. Black, R. J. England, L. Su, R. Trivedi, Y. Miao, O. Solgaard *et al.*, Science **367**, 79 (2020).
[17] R. Shiloh, J. Illmer, T. Chlouba, P. Yousefi, N. Schönenberger, U. Niedermayer, A. Mittelbach, and P. Hommelhoff, Nature (London) **597**, 498 (2021).
[18] T. Fishman, U. Haeusler, R. Dahan, M. Yannai, Y. Adiv, T. L. Abudi, R. Shiloh, O. Eyal, P. Yousefi, G. Eisenstein *et al.*, Nat. Commun. **14**, 3687 (2023).
[19] T. Chlouba, R. Shiloh, S. Kraus, L. Brückner, J. Litzel, and P. Hommelhoff, Nature (London) **622**, 476 (2023).
[20] C. Roques-Carmes, N. Rivera, A. Ghorashi, S. E. Kooi, Y. Yang, Z. Lin, J. Beroz, A. Massuda, J. Sloan, N. Romeo *et al.*, Science **375**, eabm9293 (2022).
[21] Y. Kurman, N. Lahav, R. Schuetz, A. Shultzman, C. Roques-Carmes, A. Lifshits, S. Zaken, T. Lenkiewicz, R. Strassberg, O. Beer *et al.*, arXiv:2302.01300.
[22] O. Kfir, Phys. Rev. Lett. **123**, 103602 (2019).
[23] V. Di Giulio, M. Kociak, and F. J. García de Abajo, Optica **6**, 1524 (2019).
[24] X. Bendana, A. Polman, and F. J. García de Abajo, Nano Lett. **11**, 5099 (2011).
[25] V. Di Giulio and F. J. García de Abajo, Optica **7**, 1820 (2020).
[26] A. Ben Hayun, O. Reinhardt, J. Nemirovsky, A. Karnieli, N. Rivera, and I. Kaminer, Sci. Adv. **7**, eabe4270 (2021).
[27] V. Di Giulio, O. Kfir, C. Ropers, and F. J. García de Abajo, ACS Nano **15**, 7290 (2021).
[28] O. Kfir, V. Di Giulio, F. J. García de Abajo, and C. Ropers, Sci. Adv. **7**, eabf6380 (2021).
[29] A. Karnieli, N. Rivera, A. Arie, and I. Kaminer, Sci. Adv. **7**, eabf8096 (2021).
[30] A. Konečná, F. Iyikanat, and F. J. García de Abajo, Sci. Adv. **8**, eabo7853 (2022).
[31] G. Baranes, R. Ruimy, A. Gorlach, and I. Kaminer, npj Quantum Inf. **8**, 32 (2022).
[32] S. Peng, N. J. Schilder, X. Ni, J. Van De Groep, M. L. Brongersma, A. Alù, A. B. Khanikaev, H. A. Atwater, and A. Polman *et al.*, Phys. Rev. Lett. **122**, 117401 (2019).
[33] Y. Pan, B. Zhang, and D. Podolsky, ACS Photonics **11**, 3563 (2024).
[34] J. Li, Y. Fang, Y. Liu *et al.*, Phys. Rev. Lett. **132**, 073801 (2024).
[35] B. Barwick, D. J. Flannigan, and A. H. Zewail, Nature (London) **462**, 902 (2009).
[36] S. T. Park, M. Lin, and A. H. Zewail, New J. Phys. **12**, 123028 (2010).
[37] F. J. García de Abajo, A. Asenjo-Garcia, and M. Kociak, Nano Lett. **10**, 1859 (2010).

[38] O. Kfir, H. Lourenço-Martins, G. Storeck, M. Sivis, T. R. Harvey, T. J. Kippenberg, A. Feist, and C. Ropers, Nature (London) **582**, 46 (2020).

[39] K. Wang, R. Dahan, M. Shentcis, Y. Kauffmann, A. Ben Hayun, O. Reinhardt, S. Tsesses, and I. Kaminer, Nature (London) **582**, 50 (2020).

[40] J.-W. Henke, A. S. Raja, A. Feist, G. Huang, G. Arend, Y. Yang, F. J. Kappert, R. N. Wang, M. Möller, J. Pan *et al.*, Nature (London) **600**, 653 (2021).

[41] Y. Yang, J.-W. Henke, A. S. Raja, F. J. Kappert, G. Huang, G. Arend, Z. Qiu, A. Feist, R. N. Wang, A. Tusnin *et al.*, Science **383**, 168 (2024).

[42] R. Dahan, A. Gorlach, U. Haeusler, A. Karnieli, O. Eyal, P. Yousefi, M. Segev, A. Arie, G. Eisenstein, P. Hommelhoff *et al.*, Science **373**, eabj7128 (2021).

[43] Y. Adiv, H. Hu, S. Tsesses, R. Dahan, K. Wang, Y. Kurman, A. Gorlach, H. Chen, X. Lin, G. Bartal *et al.*, Phys. Rev. X **13**, 011002 (2023).

[44] A. Feist, G. Huang, G. Arend, Y. Yang, J.-W. Henke, A. S. Raja, F. J. Kappert, R. N. Wang, H. Lourenço-Martins, Z. Qiu *et al.*, Science **377**, 777 (2022).

[45] G. M. Vanacore, I. Madan, G. Berruto, K. Wang, E. Pomarico, R. Lamb, D. McGrouther, I. Kaminer, B. Barwick, F. J. García de Abajo *et al.*, Nat. Commun. **9**, 2694 (2018).

[46] G. Huang, N. J. Engelsen, O. Kfir, C. Ropers, and T. J. Kippenberg, PRX Quantum **4**, 020351 (2023).

[47] G. Baranes, S. Even-Haim, R. Ruimy, A. Gorlach, R. Dahan, A. A. Diringer, S. Hacohen-Gourgy, and I. Kaminer, Phys. Rev. Res. **5**, 043271 (2023).

[48] R. Dahan, G. Baranes, A. Gorlach, R. Ruimy, N. Rivera, and I. Kaminer, Phys. Rev. X **13**, 031001 (2023).

[49] A. Karnieli, S. Tsesses, R. Yu, N. Rivera, A. Arie, I. Kaminer, and S. Fan, PRX Quantum **5**, 010339 (2024).

[50] F. J. Garcia-Vidal, C. Ciuti, and T. W. Ebbesen, Science **373**, eabd0336 (2021).

[51] See Supplemental Material at http://link.aps.org/supplemental/10.1103/PhysRevLett.134.043803 for (1) the derivation of quantum interaction strength, (2) the scattering $\mathbb{T}$ matrix, (3) line-electron and (4) point-electron upper limit, (5) cutoff condition of the line-electron upper limit, (6) optimal condition of the point-electron upper limit, (7) calculations of energy loss, (8) validation of line-electron upper limit, (9) integration interval choice, (10) tightness of the bound, (11) breakdown of the limit under multimode conditions, (12) magnetic fields, (13) practical limitations, and (14) discussions on various spectral regimes.

[52] Y. Yang, A. Massuda, C. Roques-Carmes, S. E. Kooi, T. Christensen, S. G. Johnson, J. D. Joannopoulos, O. D. Miller, I. Kaminer, and M. Soljačić, Nat. Phys. **14**, 894 (2018).

[53] H. Shim, L. Fan, S. G. Johnson, and O. D. Miller, Phys. Rev. X **9**, 011043 (2019).

[54] O. D. Miller, Fundamental limits to near-field optical response, in *Advances in Near-Field Optics*, edited by R. Gordon (Springer International Publishing, Cham, 2023), pp. 25–85.

[55] L. Zhang, F. Monticone, and O. D. Miller, Nat. Commun. **14**, 7724 (2023).

[56] R. Carminati and J. C. Schotland, *Principles of Scattering and Transport of Light* (Cambridge University Press, Cambridge, England, 2021).

[57] P. Chao, B. Strekha, R. Kuate Defo, S. Molesky, and A. W. Rodriguez, Nat. Rev. Phys. **4**, 543 (2022).

[58] R. Remez, A. Karnieli, S. Trajtenberg-Mills, N. Shapira, I. Kaminer, Y. Lereah, and A. Arie, Phys. Rev. Lett. **123**, 060401 (2019).

[59] C. Luo, M. Ibanescu, S. G. Johnson, and J. Joannopoulos, Science **299**, 368 (2003).

[60] H. Andrews and C. Brau, Phys. Rev. ST Accel. Beams **7**, 070701 (2004).

[61] V. Kumar and K.-J. Kim, Phys. Rev. E **73**, 026501 (2006).

[62] Z. Wang, K. Yao, M. Chen, H. Chen, and Y. Liu, Phys. Rev. Lett. **117**, 157401 (2016).

[63] D. Pan and H. Xu, Phys. Rev. Lett. **130**, 186901 (2023).

[64] F. J. García de Abajo, ACS Nano **7**, 11409 (2013).

[65] F. Liu, L. Xiao, Y. Ye, M. Wang, K. Cui, X. Feng, W. Zhang, and Y. Huang, Nat. Photonics **11**, 289 (2017).

[66] N. Talebi, Phys. Rev. Lett. **125**, 080401 (2020).

[67] M. Liebtrau, M. Sivis, A. Feist, H. Lourenço-Martins, N. Pazos-Pérez, R. A. Alvarez-Puebla, F. J. García de Abajo, A. Polman, and C. Ropers, Light Sci. Appl. **10**, 82 (2021).

[68] S. Huang, R. Duan, N. Pramanik, J. S. Herrin, C. Boothroyd, Z. Liu, and L. J. Wong, Nat. Photonics **17**, 224 (2023).

[69] A. Karnieli and S. Fan, Sci. Adv. **9**, eadh2425 (2023).

[70] J. Chen, R. Chen, F. Tay, Z. Gong, H. Hu, Y. Yang, X. Zhang, C. Wang, I. Kaminer, H. Chen *et al.*, Phys. Rev. Lett. **131**, 113002 (2023).

[71] M. Eldar, Z. Chen, Y. Pan, and M. Krüger, Phys. Rev. Lett. **132**, 035001 (2024).

[72] R. Shiloh, T. Chlouba, and P. Hommelhoff, Phys. Rev. Lett. **128**, 235301 (2022).

[73] T. P. Rasmussen, Á. R. Echarri, J. D. Cox, and F. J. García de Abajo, Sci. Adv. **10**, eadn6312 (2024).

[74] D. Roitman, A. Karnieli, S. Tsesses, Z. Barkay, and A. Arie, Opt. Lett. **49**, 2013 (2024).

[75] V. Di Giulio, E. Akerboom, A. Polman, and F. J. García de Abajo, ACS Nano **18**, 14255 (2024).

[76] E. Akerboom, V. Di Giulio, N. J. Schilder, F. J. García de Abajo, and A. Polman, ACS Nano **18**, 13560 (2024).

[77] A. Karnieli, C. Roques-Carmes, N. Rivera, and S. Fan, ACS Photonics **11**, 3401 (2024).

[78] A. P. Synanidis, P. A. D. Gonçalves, C. Ropers, and F. J. García de Abajo, Sci. Adv. **10**, eadp4096 (2024).

[79] M. Sirotin, A. Rasputnyi, T. Chlouba, R. Shiloh, and P. Hommelhoff, arXiv:2405.06560.

[80] Y. Yang, D. Zhu, W. Yan, A. Agarwal, M. Zheng, J. D. Joannopoulos, P. Lalanne, T. Christensen, K. K. Berggren, and M. Soljačić, Nature (London) **576**, 248 (2019).

[81] P. Gonçalves and F. J. García de Abajo, Nano Lett. **23**, 4242 (2023).

[82] W. Zhu, R. Esteban, A. G. Borisov, J. J. Baumberg, P. Nordlander, H. J. Lezec, J. Aizpurua, and K. B. Crozier, Nat. Commun. **7**, 11495 (2016).

[83] A. Ciccotelli, R. B. Appleby, F. Cerutti, K. Bilko, L. S. Esposito, R. G. Alia, A. Lechner, and A. Tsinganis, Phys. Rev. Accel. Beams **26**, 061002 (2023).

[84] R. Yu, A. Konečná, and F. J. García de Abajo, Phys. Rev. Lett. **127**, 157404 (2021).

[85] F. R. Prudêncio and M. G. Silveirinha, Phys. Rev. B **98**, 115136 (2018).

[86] A. Fallah, Y. Kiasat, M. G. Silveirinha, and N. Engheta, Phys. Rev. B **103**, 214303 (2021).

[87] Z. Zhao, following Letter, Phys. Rev. Lett. **134**, 043804 (2025).

[88] A. R. Echarri, P. Gonçalves, C. Tserkezis, F. J. García de Abajo, N. A. Mortensen, and J. D. Cox, Optica **8**, 710 (2021).

[89] J. A. Van Vechten, Phys. Rev. **182**, 891 (1969).

[90] J. D. Caldwell, L. Lindsay, V. Giannini, I. Vurgaftman, T. L. Reinecke, S. A. Maier, and O. J. Glembocki, Nanophotonics **4**, 44 (2015).

[91] A. D. Rakić, Appl. Opt. **34**, 4755 (1995).

End Matter

Appendix: Limit validations—We validate the derived upper limits in Figs. 5(a)–5(c) (see calculation details in SM, Sec. S9).

We first consider two analytical scenarios: point electron interacts with the fundamental dipolar mode of an isolated sphere [Fig. 5(a)] and launch surface plasmon polaritons above a metallic half-space [Fig. 5(b)] in vacuum. Both cases permit analytical treatment of energy loss (see in SM, Sec. S7) to validate the point-electron [Eq. (7)] upper limits. In both cases, the analytical results closely trail the upper limits at the considered separation. We also numerically validate the upper limit using full-wave simulations in Fig. 5(c), where an electron passes above an integrated Si waveguide embedded in SiO_2 substrate. The numerical $|g_Q|$ of the fundamental mode falls short of the upper limit by about 1 order of magnitude. Additionally, we validate the line-electron [Eq. (6)] limit in SM, Sec. S8.

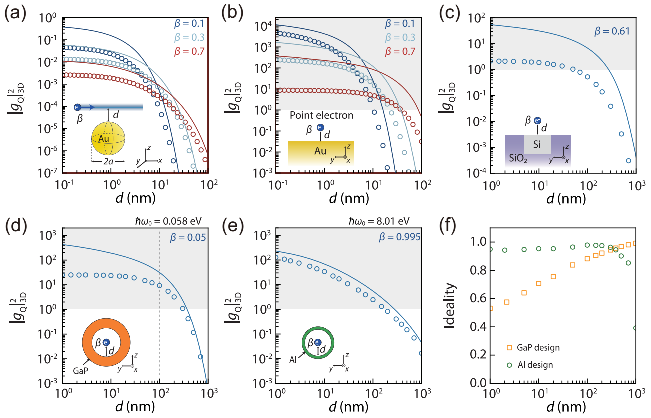

FIG. 5. Validations (a)–(c) of the theoretical upper limits and near-optimal designs (d)–(f). (a),(b) Analytical calculations compared to upper limits. A point electron couples with an isolated Drude sphere (a) of radius $a = 5$ nm and a Drude half-space (b). The Drude parameters in (a) and (b) are $\epsilon_m = 1 - \omega_p^2/\omega(\omega + i\gamma_m)$, $\omega_p = 9.06$ eV, $\gamma_m = 0.071$ eV [88] for gold. (c) Numerical simulations compared to the upper limits. A point electron moves above a Si-SiO_2 waveguide (thickness 220 nm and width 500 nm) at a distance d. (d) Near-optimal electron-photon coupling design for slow electrons: an air-GaP (Gallium Phosphide) core-shell structure with a 40 nm GaP shell. The property of polar dielectric GaP is described by a Lorentz oscillator model, $\epsilon_d = \epsilon_\infty + \epsilon_\infty(\omega_{LO}^2 - \omega_{TO}^2)/(\omega_{TO}^2 - \omega^2 - i\omega\gamma_d)$, where background permittivity $\epsilon_\infty = 9.1$ [89], $\gamma_d = 1.25$ meV, longitudinal optical ω_{LO} and transverse optical ω_{TO} phonon frequencies are 67.8 meV and 47.1 meV, respectively [90]. (e) Near-optimal electron-photon coupling design for fast electrons: an air-aluminum core-shell structure with a 13 nm aluminum [91] shell. The light gray shows the $|g_Q| > 1$ regime (circles, exact calculations; lines, theoretical upper limit). (f) The coupling ideality as a function of separation (orange squares, GaP design; green circles, aluminium design). The interaction length is fixed at 100 μm for all calculations.

We design two near-optimal core-shell structures [Figs. 5(d)–5(f); see comparison of the bound tightness in SM, Sec. S10] to verify the two predicted optimal regimes [two bright areas in Fig. 5(b)] associated with slow and fast electrons, respectively. The core-shell configuration is motivated by the sum-rule constraint constant τ, which is maximum when the largest possible near-field area of a source is occupied by the polarizable material. For the slow-electron optimum, we utilize a Lorentz polar dielectric gallium phosphide (GaP) with low optical phonon frequencies to allow the coupling between 0.058 eV infrared photons and nonrelativistic $\beta = 0.05$ electrons; for the fast-electron optimum, we adopt aluminium that features a high plasma frequency to achieve an efficient interaction between 8.01 eV ultraviolet photons and $\beta = 0.995$ relativistic electrons. In both cases, $|g_Q| > 1$ is predicted possible by the upper limits and is validated by the slightly trailing concrete designs at the separation 100 nm [dashed vertical lines in Figs. 5(d) and 5(e)] and interaction length 100 μm. In Figs. 5(d) and 5(e), GaP and aluminium, two lossy materials, are used to verify the two optimal regimes [Fig. 2(c)], as their material properties facilitate the coupling of electrons and photons at the desired energy. Alternatively, lossless platforms [e.g., Fig. 5(c)] can be employed to maintain the entanglement of the interaction.

In addition, Fig. 5(f) depicts the coupling ideality of the two near-optimal designs as the function of separation. The ideality of the target mode m is defined as $I_m = |g_{Q,m}|^2/\sum_i |g_{Q,i}|^2$, which describes the fraction of coupling into the designated mode among excitations of all modes [23,46,77] (see calculation details and discussions in SM, Secs. S9.C and S9.D). The ideality of the slow-electron design [Fig. 5(d); orange squares in Fig. 5(f)] grows monotonically with the considered separation, reaching more than 95% under $d > 500$ nm due to the dominance of the fundamental mode. Meanwhile, the fast-electron design [Fig. 5(e); green circles in Fig. 5(f)] exhibits a good ideality $> 80\%$ for a wide range of separations, including both near and far field of the 8.01 eV photon.